

Computational Fluid Dynamics Modeling and Analysis of Silica Nanoparticle Synthesis in a  
Flame Spray Pyrolysis Reactor

*Debolina Dasgupta<sup>1,\*</sup>, Pinaki Pal<sup>1</sup>, Roberto Torelli<sup>1</sup>, Sibendu Som<sup>1</sup>, Noah Paulson<sup>2</sup>, Joseph  
Libera<sup>2</sup>, Marius Stan<sup>2</sup>*

<sup>1</sup>*Energy Systems Division, Argonne National Laboratory, 9700 S. Cass Ave, Lemont, IL-60439*

<sup>2</sup>*Applied Materials Division, Argonne National Laboratory, 9700 S. Cass Ave, Lemont, IL-60439*

*\*Corresponding Author Email: [ddasgupta@anl.gov](mailto:ddasgupta@anl.gov)*

Corresponding author: Debolina Dasgupta

Corresponding author email: [ddasgupta@anl.gov](mailto:ddasgupta@anl.gov)

Corresponding author address: 9700 S. Cass Ave, Lemont, IL-60439

Type of article: Full-length

## **Abstract**

Flame Spray Pyrolysis (FSP) is a method for large-scale production of nanoparticles and nanoscale powders employed in a wide range of industrial applications. Particle size and morphology are complex functions of the physicochemical phenomena occurring in the FSP reactor. An extensive study of FSP-related phenomena can be utilized to develop effective strategies for achieving desired particle size/morphology and scaling up the overall yield of an FSP system. In this work, a computational fluid dynamics (CFD) model of an FSP reactor is developed to simulate the coupling of key phenomena involved in the particle synthesis process: liquid spray breakup and evaporation, mixing, combustion, and particle formation/growth of silica nanoparticles. The particle sizes and their distributions from the CFD simulations are validated against experimental data. Subsequently, the simulations are utilized to investigate the impact of process parameters on the resultant flame dynamics and particle growth. Firstly, the CFD results show that the particle sizes are strongly correlated with the precursor concentration in the solvent. At lower precursor concentrations, the spread of the distribution is relatively insensitive to the value of the concentration. At higher concentrations, the spread is higher as the collision probability between particles is higher. Secondly, increasing the pilot flow rate increases the length of the pilot flames impacting the local ignition location of the spray flame. Lastly, it is shown that the dispersion gas flow rate strongly influences the spray flame shape. This shape can be used for control of particle growth as it helps determine the regions of high temperature and the residence time of the particles in the high temperature region enabling the design and process optimization of the FSP reactor.

***Keywords: Flame spray pyrolysis, Multiphase turbulent reacting flows, Computational fluid dynamics, Numerical modeling, Nanoparticle synthesis***

## 1. Introduction

Nanoparticles are employed for a wide range of industrial applications, such as catalysts, battery materials, biomedical imaging, energetics, etc. Flame spray pyrolysis (FSP) is a versatile, cost-effective, and scalable method for large-scale production of single and multi-component oxide nanoparticles (e.g.,  $\text{SiO}_2$ ,  $\text{TiO}_2$ ,  $\text{FeO}$ ,  $\text{Al}_2\text{O}_3$ ) from relatively inexpensive precursors [1]. The process allows for strict control of the particle size and its distribution, and can continuously produce highly pure and thermally stable particles requiring minimal after-treatment [2]. The FSP method also offers great flexibility in terms of choice of precursors and flow controls, which in turn determine the amount of material produced. The particle formation can be described by a series of complex phenomena – namely, precursor atomization, droplet evaporation, spray combustion, particle nucleation, growth, agglomeration, and sintering. The size of the flame-generated particles ranges from a few to several hundred nanometers, depending on the operating conditions. It is well known that the final particle size and its morphology are strong functions of the flame temperature, residence time of the particles in the flame, local precursor concentration, dispersion gas flow rate, and the flow field within the reactor [3]. However, the nature of interactions among the fluid dynamics, chemistry, and mechanisms of nanoparticle formation is not sufficiently well understood. Due to the complexity of the physical and chemical phenomena involved in the controlled FSP synthesis, the influence of the operating conditions (flow field, spatial scalar distribution, precursor typology, oxidant typology, spray atomization) on the final product (i.e., morphological and structural properties of the derived nanoparticles) needs to be investigated.

A typical FSP process is comprised of a central nozzle that injects a solution of a precursor (typically containing the metal or metalloid of choice such as silicon, titanium, iron, etc.) and a solvent (e.g., ethanol, acetonitrile, o-xylene, etc.). The nozzle is surrounded by a fast co-flowing dispersion gas (air or pure oxygen) which enhances the atomization of the liquid solution and provides the necessary oxidizer for combusting the liquid mixture. Adjacent to the dispersion gas, sheath gas is introduced. Sheath gas, air or oxygen, helps stabilize the spray flame and provides additional oxidizer for the spray flame. Most precursors have low combustion enthalpy leading to endothermic reactions that do not form self-sustaining flames [1]. Therefore, an external flame source, usually oxy-hydrogen or oxy-hydrocarbon, is required to support the combustion. The droplets resulting from the near-nozzle atomization are vaporized and ignited by this supporting

pilot flame resulting in a spray flame. The high temperatures within this flame lead to the formation of nanoparticles through the processes of nucleation, coagulation, sintering, and/or surface growth. A variety of products can be synthesized using FSP, such as zinc oxide [4], titanium oxide [5], and zirconium oxide [6]. Silica nano-powders are also commonly produced from flame synthesis using inorganic (e.g., silicon tetrachloride) and organic (e.g., tetraethylorthosilicate (TEOS), tetramethylorthosilicate (TMOS)) silicon compounds. Due to the highly complex nature of FSP, many diagnostics, such as X-rays, transmission electron microscopy (TEM), scanning mobility particle size (SMPS), particle mass spectrometer (PMS), have been applied to characterize the associated particle diameter and its distribution [3, 7-10]. Other techniques are used for characterizing the spray droplets and spray flame. Spray droplet sizes and velocity profiles have been estimated using Mie scattering [11], high-speed shadowgraph imaging, and phase Doppler anemometry (PDA) [10]. Coherent Anti-Raman Stokes Spectroscopy (CARS) [10-12], OH\*, CH\* and SiO\* 2-D chemiluminescence [11], and other diagnostics outlined by Schulz et al. [8] have been used to obtain spatial distribution of the spray flame's temperature and shapes. As far as computational studies are concerned, while the reacting flow and Lagrangian spray modeling are fairly well established, a significant body of work has focused on developing strategies to model the nanoparticle evolution. The latter is generally described by the general dynamics equation (GDE) [13] which yields a continuous distribution function. The GDE describes the convection, diffusion, nucleation, surface growth, coagulation, and coalescence of the particles. Several methods to solve the GDE have been proposed in the past. Discrete models [14] introduce differential equations for discrete sizes or particle properties (such as number density, surface area, etc.), whereas Sectional methods [15] solve for particles of different size classes by introducing a differential equation for each section. Discrete models, such as the Method of Moments (MOM) and modified MOM, have been used to describe the size distribution of moments for the particle size distribution [16-19]. A simplified single-moment or monodisperse model, proposed by Kruis et al. [20], introduces transport equations for number density, volume, and surface area, and has been extensively used in numerical studies to simulate synthesis of ZrO<sub>2</sub> [21], TiO<sub>2</sub> [5], and SiO<sub>2</sub>[22]. Due to the complexity of the system, computational modeling of the FSP system is relatively limited. Two dimensional and three dimensional Reynolds-averaged Navier-Stokes (RANS) simulations have been performed by Weise et al. [5], Grohn et al. [21], Noriler et al. [23], Neto et al. [24], and Meierhofer et al. [10]. Rittler et al. [22] presented one of the first Large Eddy

Simulations (LES) of the FSP system for silica nanoparticles. A coordinated initiative in Germany has led to the development of the SpraySyn burner [25] with the goal of adding benchmark data to the literature for the development of effective models for nanoparticle formation in spray flames. LES of this burner has been performed by Wollny et al. [26] for platinum nanoparticles and Schneider et al. [25] for iron oxide nanoparticles. Recently, Abdelsamie et al. [27] conducted the first Direct Numerical Simulations (DNS) of the SpraySyn burner for TiO<sub>2</sub> production. Since then a few other DNS studies have emerged for nanoparticle formation in premixed and non-premixed flames [28] and for the impact of injector geometry for turbulent spray combustion in the SpraySyn burner [29].

The operating conditions of the FSP reactor have a significant influence on the material synthesis process. These include the liquid feed rate, dispersion gas flow rate, sheath gas flow rate, and pilot flow rate. For example, Mueller et al. [30] observed an increase in spray flame height with increasing liquid feed for SiO<sub>2</sub> particle synthesis. This dependence of flame height on the liquid feed rate has been observed for other particles as well [10, 31]. Increasing the sheath oxygen flow rate tends to dilute the spray flame. This, in turn, leads to reduced particle collisions, coalescence, and growth resulting in overall smaller particles. However, this effect can be controlled by altering the geometry of the burner [30, 32]. As stated earlier, the typical choices for the dispersion gas include air and oxygen. It has been noted that using air as dispersion gas tends to produce longer spray flames compared to those that use oxygen, leading to increased particle production rates. However, reducing the oxygen content leads to lower flame temperature and smaller particles [31, 33]. Bieber et al. [34] performed an experimental study with an angled dispersion gas and showed that this geometry produces smaller spray droplets leading to enhanced flame stability. Other studies reported a strong dependence of particle diameter on the precursor concentration and showed that increasing said concentration leads to larger particle sizes [30, 32]. This is attributed to a higher particle concentration in high-temperature regions resulting in increased particle coalescence. In fact, Mädler et al. [35] demonstrated the ability to control the size of the FSP-made particles by regulating the oxidant flow rate and precursor concentration.

In the context outlined so far, this work presents a combined experimental and computational study focused on particle synthesis of silica particles in an FSP reactor. To this end, a 3-D computational fluid dynamics (CFD) model was developed to simulate FSP and particle synthesis in the FSP reactor at Argonne National Laboratory's Materials Engineering Research Facility (MERF). This

work focuses on the flow and flame dynamics within this realistic reactor. Simulations were performed for selected inflow conditions and validated against experimental data by comparing the CFD-predicted particle size and distribution with the experimental counterparts. Next, the impact of the pilot flow rates and dispersion gas flow rate on the spray flame behavior is investigated.

This manuscript is organized as follows. First, the experimental setup and the computational models are reported in detail. Thereafter, results from the numerical simulations are presented along with validation studies against experimental data, and the effects of precursor concentration. The latter result sub-sections focus on the flame and flow dynamics of the FSP system and the influence of the pilot flow rate, and dispersion flow rate on the spray flame behavior is analyzed. Finally, the manuscript concludes with a summary of the main findings and future directions.

## **2. Methods**

### **2.1 Experimental setup**

The FSP experiments were performed at Argonne's MERF using an experimental setup similar to the one described by Mädler et al. [35]. A schematic of the FSP burner is shown in Figure 1. In this configuration, a mixture of precursor and solvent is injected through a single-hole nozzle whose diameter is 0.5 mm. The dispersion oxygen is introduced through four grooves on the liquid injector insert, arranged at an angle of 15° with respect to the insert's axis. The liquid insert is enclosed by a swirl channel. This geometry results in a complex dispersion oxygen flow field with four high-velocity swirling oxygen jets with an additional radially inward motion due to the converging geometry. The jets eventually enter the reactor through an opening of 0.38 mm. The sheath oxygen is introduced through an annulus of width 1.525 mm, 8 mm from the center of the geometry. The premixed methane/oxygen reactant mixture for the pilot flame is introduced through six ports of 0.889 mm diameter and placed in a hexagonal pattern at a distance of 14.79 mm from the center. Finally, nitrogen gas flow is established from an annulus of width 41.275 mm located 31.75 mm from the center. The reactor is encased in a cylindrical domain of total length 304.8 mm and diameter 146.05 mm.

A liquid solution of TEOS (pure, Merck KGaA, Germany) in reagent ethanol alcohol (C<sub>2</sub>H<sub>5</sub>OH 94.0–96.0% VWR Chemicals BDH, USA) was combusted using an oxygen atomizing nozzle (Schlick Nozzle Model 970 S8, D4.1016/1 Version 1.0, Germany). Table 1 summarizes the operating conditions (at 1 atm, 20°C) considered in the present work.

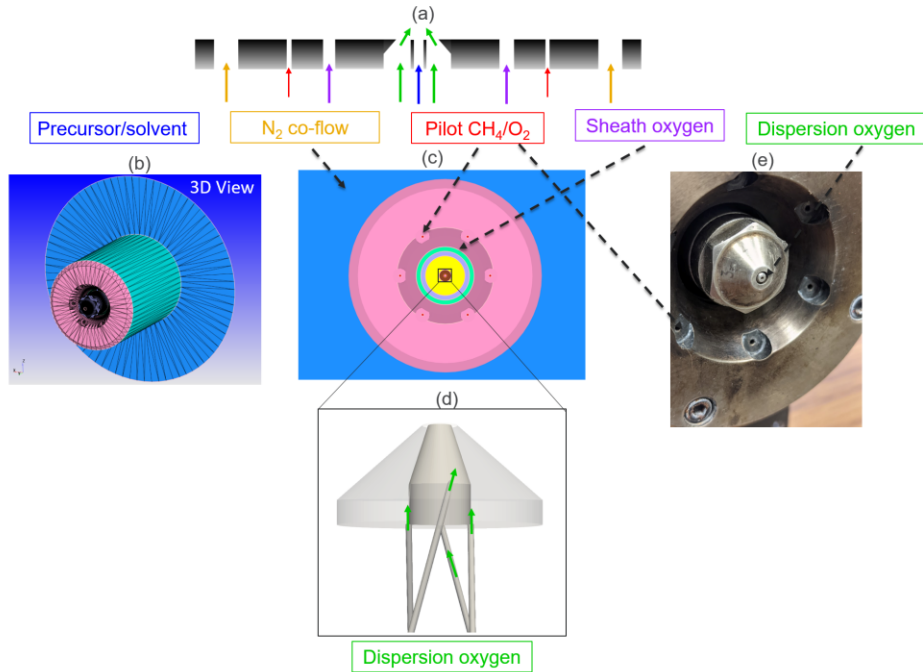


Figure 1. (a) Schematic of the FSP burner. The color of the arrows matches the color of the labels; (b) 3D view of the burner geometry; (c) Front view of the burner geometry; (d) zoomed view of the injector pintle and swirling channel with direction of dispersion oxygen marked in green; (e) close-up image of the FSP system showing the nozzle, pilot burners, and swirl channel.

Table 1. Flow rates for different operating conditions.

Case #	$\dot{m}_{pilot}$ [L/min]	$\dot{m}_{disp,O_2}$ [L/min]	$\dot{m}_{sheath,O_2}$ [L/min]	$\dot{m}_{liq}$ [mL/min]	TEOS Concentration [%-vol]
1	3.2	9.3	24	7.3	7.95
2	6.0	6.3	17	4.3	1.26
3	6.3	11.7	18	9.7	0.5
4	7.2	10.5	15	8.5	0.2

Particle sizes were measured by a scanning mobility particle sizer (SMPS) (TSI Model 3082 Electrostatic Classifier with Model 3776 Ultrafine Condensation Particle Counter, USA). The SMPS instrument ingests a constant flow of 1.5 LPM. A crossflow in the collection tube controls the ingestion of aerosol laden exhaust through a 0.03” diameter hole at the center of tube facing the exhaust flow. The secondary nitrogen dilution flow was selected to be 1.35 LPM so that the sampling was ingested at 1.5-1.35 = 0.15 LPM. This was found to be sufficient to lower the dew

point of the exhaust gas so that condensation of water was avoided in the sampling tube. The diluted aerosol stream was transported to the SMPS instrument using a 60" long ¼ ID anti-static tubing provided by TSI instruments. At the instrument, the sample stream was passed through a particle impactor to remove particles greater than 1 micron. Samples were analyzed continuously at 2 min spacing between scans. A data analysis procedure was developed to extract an analytical form of the particle size distribution using particle counts within discrete size bins measured by the SMPS. The SMPS device received a continuous stream of samples that was sorted by an electrostatic classifier and then counted by a condensation particle sampler. The SMPS data is fit to a lognormal distribution as the range of measurement of the SMPS device is limited. By fitting the lognormal distribution to the range of measured data, the tails of the distribution and the distribution's moments (mean, standard deviation) can be estimated. Firstly, each unphysically low count was removed if it accounted for less than 0.1% of the maximum count, for any particle size bin. Using a five-element averaging window, the distribution was further smoothed followed by a normalization by the maximum count. The log-normal distribution characterized by the mean, standard deviation, and shape parameters was found to closely match the available range of particle sizes in most cases. Next, the differential evolution global optimization scheme available in the open source SciPy Python [36] package was employed to identify parameter values that minimized the mean squared error between the measurements and fit. Further details of this methodology can be found in Paulson et al. [37].

## **2.2 Computational model for the FSP burner**

The CONVERGE CFD software [38] was used to perform unsteady Reynolds-averaged Navier-Stokes (RANS) simulations of the FSP reactor using a compressible flow solver. Four separate cases with the different operating conditions listed in Table 1 are simulated for the current study. The overall domain size for each case is 304.8 mm x 146.05 mm x 146.05 mm with the geometric details of all in the internal components listed in Section 2.1. The finite-rate-chemistry-based well stirred reactor combustion model is implemented. The chemical kinetics from a merged mechanism of Marinov et al. [39] and a multi-step pyrolysis and oxidation mechanism for TEOS [40], with 64 species and 392 reactions was employed to model the combustion phenomena. The methane/oxygen flames were ignited using a spherical 0.1 J energy source of radius 3 mm. For turbulence closure, the Re-Normalization Group (RNG)  $k$ - $\epsilon$  turbulence model [41] was used. The

base grid size for this setup was 2 mm. The regions around the liquid insert, within the swirling channel, around the sheath oxygen exit and the pilot flame burner are provided with additional refinement with a minimum grid size of 0.25 mm to ensure all flow paths and boundaries are effectively resolved. In addition, adaptive mesh refinement based on local gradients of velocity and temperature was applied resulting in a minimum mesh size of 0.25 mm for the entire domain. The limiting time step is based on the convective Courant-Fredrich-Lewy (CFL) number and is of the order of  $10^{-7}$  s with CFL=0.7. The different flows were prescribed using mass-flow-based inflow boundary conditions. The top of the domain is prescribed an atmospheric pressure outflow boundary condition. All other boundaries are treated as a no-slip adiabatic wall. A schematic of the geometry with the marked domain lengths and inflow and outflow boundary conditions are shown in Figure 2. The velocities and the turbulent fluctuations at the exit of the swirl channel are high leading to Reynolds number of the order of 50,000 near the nozzle exit.

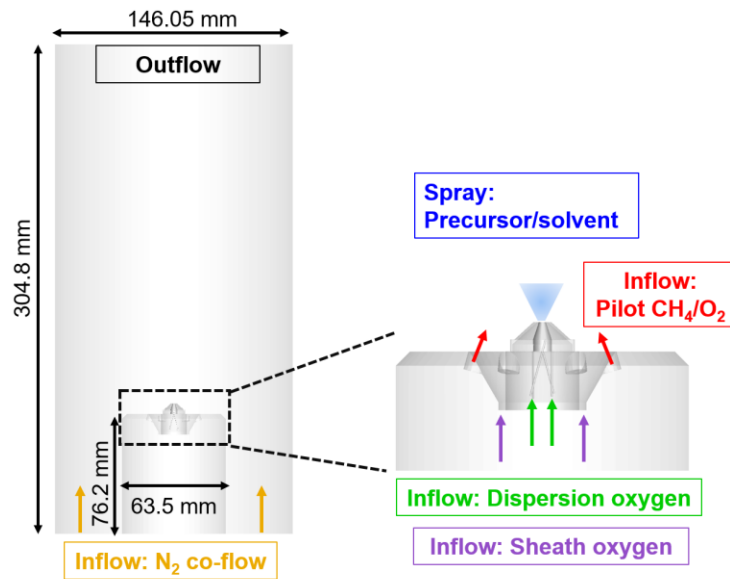


Figure 2. Schematic of the full FSP reactor showing the domain size and the inflow, outflow boundary conditions. The zoomed image of the FSP system shows the different inflow boundaries prescribed by the values in Table 1. The color of the arrows correspond to color of the text to indicate the type of inflow.

The primary atomization of the spray was modeled via volume-of-fluid (VOF) [42] large eddy simulations (LES) of the injection and dispersion oxygen systems, as discussed later. The High-Resolution Interface Capturing (HRIC) model with two-phase momentum conservation [43] was

employed to predict the primary atomization process. These simulations were used to extract estimates of the droplet size distribution near the nozzle exit for the initialization of a solid-cone Lagrangian spray via a Rosin-Rammler distribution in the subsequent decoupled FSP reactor RANS simulations. Detailed temperature-dependent thermo-physical properties (e.g., heat of vaporization, viscosity, surface tension, etc.) were used for both species in the solvent/precursor mixture. The Taylor Analogy Breakup (TAB) model [44] was employed to describe the secondary droplet breakup of the Lagrangian spray. The droplet evaporation is modeled using the Frossling model [45] and the multi-component droplets evaporate into their base species. Nanoparticle formation was modeled using the hybrid method of moments (HMOM) [13] with four moments. Particle nucleation leads to the generation of the primary particles with SiO<sub>2</sub> as the precursor species. The nucleation rate was calculated by the rate of formation of SiO<sub>2</sub>, using the forward reaction rates for reactions with SiO<sub>2</sub> as product. This estimation assumes an immediate formation of the SiO<sub>2</sub> monomers. Similar assumptions have been made in previous studies [5, 22]. The coagulation and coalescence phenomena were modeled using a collision frequency function dictating exchange of particles between difference size classes [46]. The surface sintering rate was accounted for by using a reaction rate,  $RR_{sintering}$ , given by:

$$RR_{sintering} = 1/\tau \quad ; \quad \tau = Ad_p \exp \left\{ \frac{B}{T} \left( 1 - \frac{d_{p,min}}{d_p} \right) \right\} \quad (1)$$

where,  $d_p$  is the particle diameter in meters,  $T$  is the temperature in K, and  $A$ ,  $B$ , and  $d_{p,min}$  are constants for a given nanoparticle. For SiO<sub>2</sub>,  $A = 6.5 \times 10^{-17}$  s/m,  $B=83000$  K,  $d_{p,min}=1$  nm [47]. This model has been validated for a simplified burner configuration [48].

### 2.3 Computational model for the VOF simulations

Due to the lack of spray diagnostics, similar to Weise et al. [5], LES of the gas-liquid interaction was performed using the VOF method [42] and the one-equation Dynamic Structure turbulence model [49] to understand the primary break-up behavior and establish spray initialization parameters for the RANS simulations. The domain inlet geometry is comprised of the injector liquid insert and the surrounding swirl channel. Liquid ethanol was introduced through a pipe of diameter 0.5 mm and length 2.5 mm. The gaseous oxygen flow was introduced through four pipes of length 10 mm attached to the insert body at an angle of 15°. The liquid and gas were injected with mass flow rates of 6 mL/min and 10 L/min, respectively, into a cylindrical domain of 20 mm

height and 20 mm diameter, as shown in Figure 3(a). The liquid and gas flow inlets are colored by the volume fraction of gas, where  $\alpha = 0$  corresponds to pure liquid and  $\alpha = 1$  corresponds to pure gas. The base grid size for this setup was 120  $\mu\text{m}$ . Adaptive mesh refinement based on local gradients of velocity and volume fraction was applied resulting in a minimum mesh size of 7.5  $\mu\text{m}$ . For the swirling channel, close to the wall, three layers of boundary-embedded refinement of 15  $\mu\text{m}$  resolution were employed. For the liquid-feed pipe, the last 0.625 mm before the exit of the channel were refined down to 7.5  $\mu\text{m}$  mesh size. For rest of the pipe length, the mesh size was kept at 15  $\mu\text{m}$ . A sample of the computational mesh is shown in Figure 3(b) and 2(c). The limiting time step is based on the convective CFL number and is of the order of  $10^{-9}$  s with CFL=0.5. Firstly, the liquid flow was established without the oxygen flow. The continuous liquid column formed disintegrates at some distance downstream of the nozzle exit. As the liquid jet moves downstream from the nozzle exit, the initially smooth liquid column develops distinct disturbances on its surface. As the amplitude of the disturbance grows, drops begin to be pinched off from the liquid column leading to an asymmetric liquid column. The liquid-only simulations are run for 10 ms (approximate time for the liquid column to reach 10 times the diameter of the nozzle i.e. 0.5 mm with an average velocity of 0.5m/s). Using this flow-field as starting point, the oxygen flow was activated and allowed to interact with the liquid column resulting in its atomization. The simulation time with the oxygen flow switched on was 6 ms. The primary atomization was fully established after 2 ms and the droplet size distribution was determined by averaging data between 4-5 ms within a cubic volume of side 8 mm near the nozzle exit. This region is also shown in Figure 3(a) using a dotted grid.

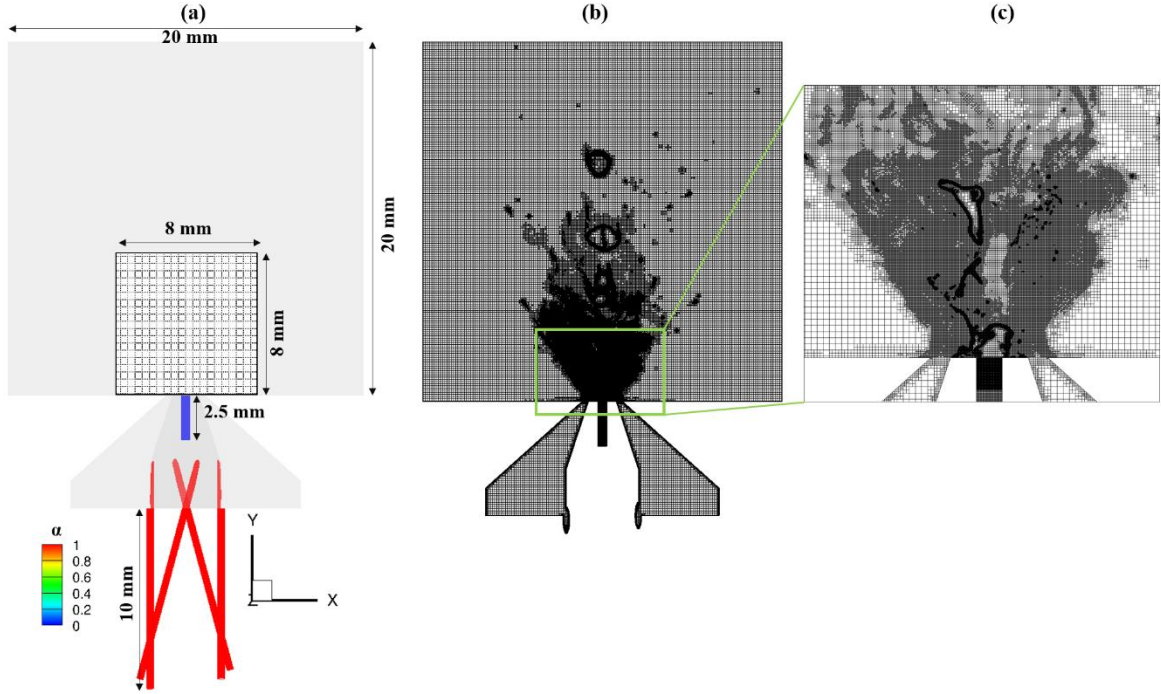


Figure 3. (a) VOF-simulation geometry with liquid and gas inflows colored by their volume fraction; (b) Slice of the computational grid at  $Z=0$  mm and  $t=4$  ms; (c) Zoomed view of the same slice focused on the liquid-feed outlet at  $t=4$  ms.

### 3 Results and Discussion

#### 3.1 Spray injection and primary break-up

The VOF simulations provide an understanding of the primary break-up behavior and spray initialization parameters for the RANS simulations of the full burner. Figure 4 shows a time sequence of the evolution of  $\alpha = 0.5$  iso-surface. The iso-surfaces are colored by the out-of-plane ( $Z$ ) velocity wherein a flow out of the X-Y plane is positive and flow into the plane is negative. The liquid Reynolds number ( $Re_l$ ) and aerodynamic Weber number ( $We_g$ ) are calculated as:

$$Re_l = \rho_l u_l d_l / \mu_l ; We_g = \rho_g (u_g - u_l)^2 d_l / \sigma_l \quad (1)$$

where,  $\rho_l$ ,  $u_l$ ,  $d_l$ ,  $\mu_l$ ,  $\rho_g$ ,  $u_g$ , and  $\sigma_l$  are the liquid density, liquid velocity, diameter of the liquid-feed pipe, liquid dynamic viscosity, gas density, gas velocity and liquid surface tension. The liquid Reynolds number and aerodynamic Weber number for this case are  $\sim 180$  and  $\sim 160$ , respectively. The reference values used for calculating these numbers are summarized in Table 2.

Table 2. Reference values for calculating non-dimensional numbers.

$\rho_l$	$u_l$	$d_l$	$\mu_l$	$\rho_g$	$u_g$	$\sigma_l$
790 kg/m <sup>3</sup>	0.5 m/s	0.5 mm	10.95 x 10 <sup>-4</sup> N-m/s	1.331 kg/m <sup>3</sup>	80 m/s	22.39 mN/m

The spray breakup regimes in externally mixing twin-fluid nozzles are given by the Hopfinger diagram [50]. Based on the  $We_g$  and  $Re_l$ , the case discussed in this work falls in the membrane-breakup regime. From Figure 4, it can be observed that the central liquid column is pulled away from the centerline by the surrounding high-velocity swirling oxygen flow, generating thin ligaments near the nozzle. Due to the aerodynamic forces, the ligament ends stretch and pinch-off. Behind this end, the ligament sheet is blown into a bag, forming a membrane. The membranes break into small droplets when the surface tension forces become of the same order as the aerodynamic forces. A similar behavior was also noted by Stodt et al. [51] for a different FSP nozzle system.

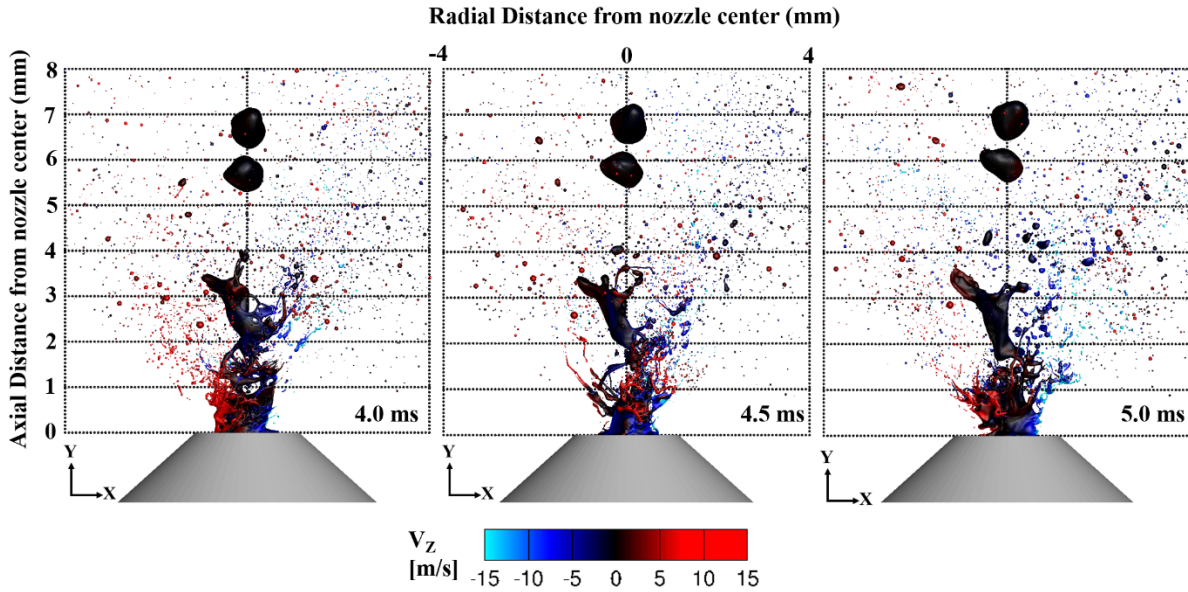


Figure 4. Iso-surfaces for  $\alpha=0.5$  colored by the Z-component of velocity at three different time instants.

The droplet size distribution was calculated using all the droplets (except the two large pinched off blobs at  $\sim 6$  and  $7$  mm since they are not formed by the oxygen flow atomization) located within the smaller cubic volume of 8-mm edge. At every time-step, each droplet was identified, and its volume, surface area, and hydraulic diameter were estimated. Using the diameters of these

droplets, the probability distribution function (PDF) and the corresponding cumulative distribution (CDF) function were calculated. Finally, the cumulative distribution, using all droplets across the 1-ms time frame, was fit to a Rosin-Rammler distribution given by the equation below:

$$CDF = 1 - \exp[-\xi^q], \quad 0 < \xi < \xi_{max} \quad (2)$$

Where  $\xi = r/\bar{r}$ ,  $\bar{r} = \Gamma(1 - q^{-1})d_{32}/2$ ,  $d_{32} = 6V_p/A_p$

Here,  $d_{32}$  is the Sauter Mean Diameter (SMD) estimated using the total volume ( $V_p$ ) and total surface area ( $A_p$ ) of all droplets,  $\Gamma$  is the gamma function, and  $q$  is the constant fit for the distribution.

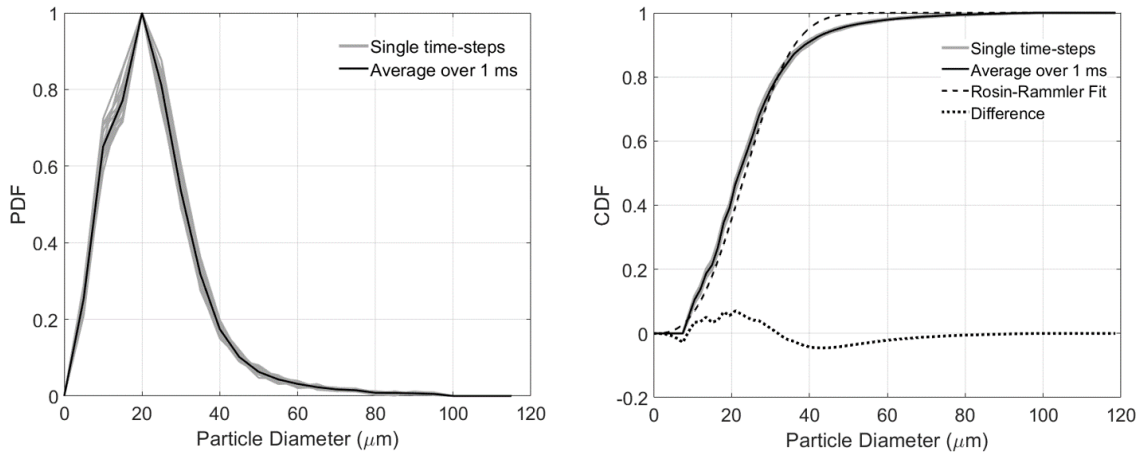


Figure 5. Probability distribution function (left) and cumulative distribution function (right) for droplet size distribution.

Figure 5 shows the PDF and CDF for different time-steps sampled at 0.05 ms, and the mean distribution over 1 ms. Overall, the PDFs have limited variability with the largest differences found in the 10-20 μm and ~40-60 μm ranges. These differences can potentially be attributed to the ligament breakup resulting, at first, in larger droplets, followed by subsequent breakup into smaller droplets. The CDFs show a lower variability compared to the PDF over different time instants. The average CDF was fit to a Rosin-Rammler distribution, using an SMD of 38.3 μm, yielding  $q = 2.86$ . These values were used to initialize the spray in the unsteady RANS simulations of the FSP reactor. The difference between the average CDF and Rosin-Rammler-fit CDF is also plotted in Figure 5, and the maximum variation was found to be around  $\pm 7\%$  for droplets in the ~15-25 μm and ~35-45 μm ranges.

The spray-angle estimation method is detailed in Figure 6. A line-of-sight integration of the gas volume fraction was performed at every time-step, resulting in a 2-D contour plot, such as the one shown in Figure 6 (a). This contour was binarized to show a liquid “existence” region wherein liquid is detected in the yellow region ( $0 \leq \alpha < 1$ ), and no liquid exist in the blue region ( $\alpha = 1$ ). These binarized contours were averaged across the 1 ms time frame and the  $c = 0.5$  contour line was identified. This contour line, signifying the spray boundary, was used to estimate the spray half angle as shown in Figure 6 (d). The asymmetry in the droplet existence region can be attributed to the asymmetric liquid column at the start of the simulations with the oxygen flow. A mean of  $\theta_{left}$  and  $\theta_{right}$  was used as the spray half-angle for the spray initialization. The parameters identified here were used to initialize all RANS simulations irrespective of the differences in liquid and atomizing oxygen flow rates. Additionally, the atomization happens close to the nozzle exit. Thus, for the RANS simulations, the spray is initialized 0.5 mm downstream of the nozzle.

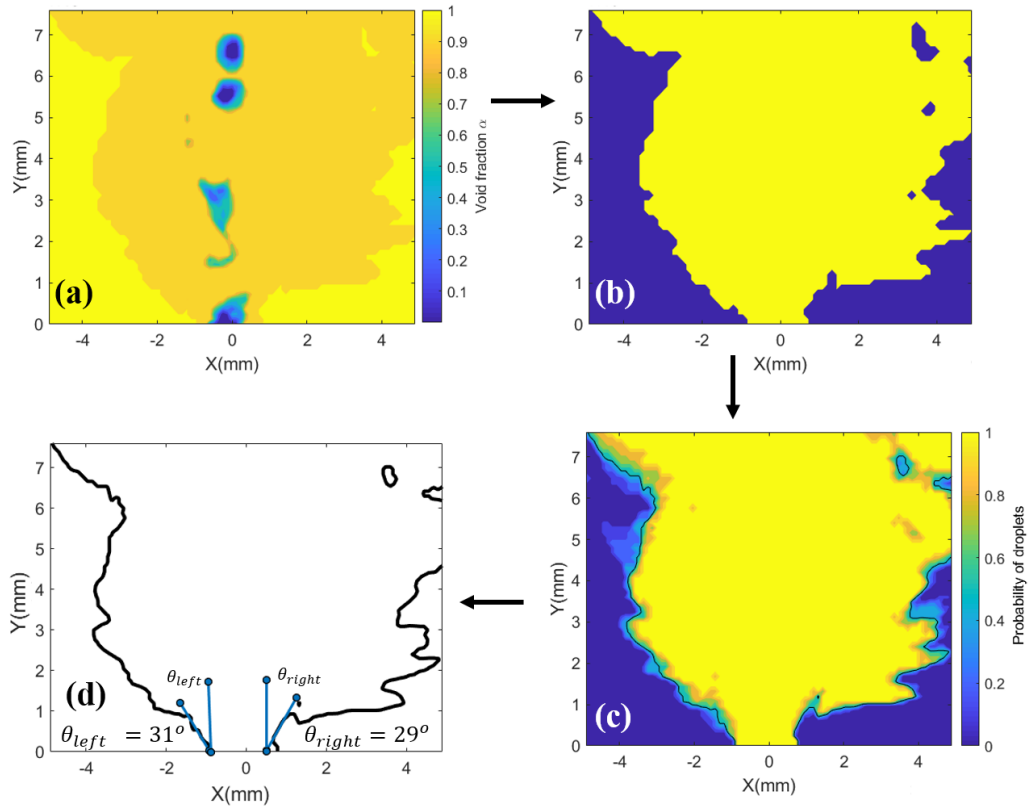


Figure 6. Spray angle estimation: (a) void fraction averaged across all Z-planes for a single time instant; (b) binarized droplet "existence" region for a single time instant; (c) binarized distribution averaged across 1 ms with  $c = 0.5$  contour line (black); and (d) half-angle estimation using  $c = 0.5$  isoline.

### **3.2 Pilot and Spray Flame ignition and evolution**

The evolution of the pilot and spray flames, and subsequent spray flame stabilization in the reactor are depicted in Figure 7 and can be described as follows. The pilot flame is first ignited with an energy source. Simultaneously, the spray is initialized 1.0 mm downstream of the nozzle using the SMD,  $q$ , and spray angle obtained in Section 3.1. The pilot flame stabilizes and evolves leading to increased temperature in the region around the spray. The higher temperature increases vaporization of the spray droplets. The fuel vapor is then ignited, thereby resulting in a spray flame in the central region. All analysis shown in the following sections is performed after the flame reaches a statistically stationary steady state. To estimate this time, the time series of the average temperature at the outflow boundary is monitored. With the spray flame ignited, as the flame evolves, the average temperature increases. Beyond a certain time, this value saturates and data from subsequent time-steps are used for analysis.

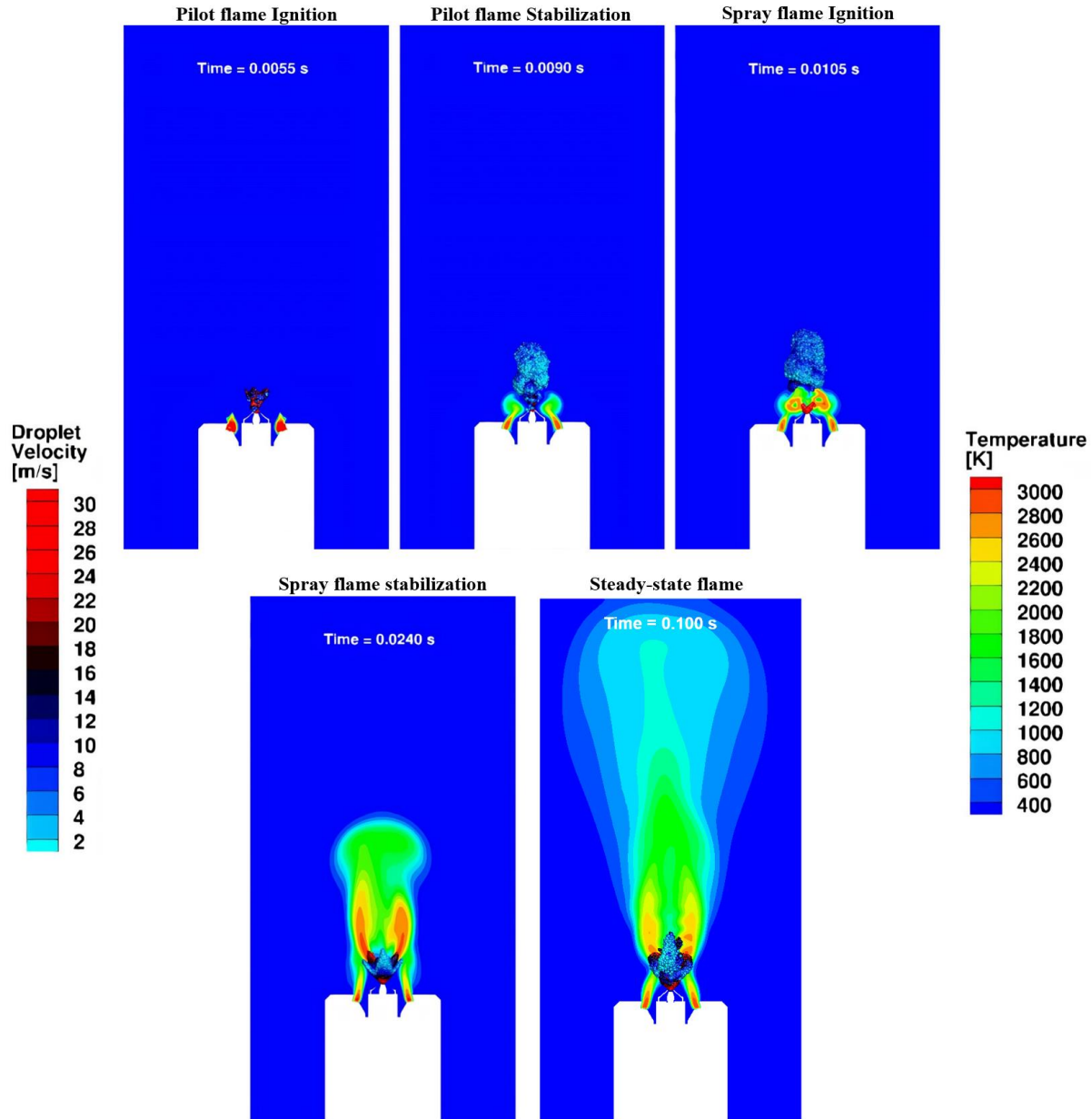


Figure 7. Pilot and spray flame ignition and stabilization shown on  $Z=0$  mm plane with temperature contours and Lagrangian droplets colored by the droplet velocity. This evolution is shown for Case 1

### 3.3 Qualitative comparison between experiments and simulations

Figure 8 (a) shows a comparison for the average flame shape. The flame shape from the simulations is represented by a line-of-sight integrated temperature contours for Case 2. The

simulation flame shape image is compared with the flame luminescence image from experiments. The high intensity region, in both cases, is observed close to the nozzle exit. Additionally, both images show an elongated spray flame in the center with decreasing intensity with increasing distance from the nozzle exit. Figure 8 (b) shows a comparison of the average reacting spray distribution close to the nozzle exit. The experimental spray image is obtained by averaging the laser scattering images of the central plane. For the simulations, the volume of the droplets are averaged at the central place. Since larger droplets scatter more light leading to higher intensity, this metric was chosen. In the RANS simulations, the spray is initialized 1 mm downstream of the nozzle exit. This choice is made as the VOF simulation show no droplets between the nozzle exit and this downstream distance. The nozzle exit, the location of the spray initialization, and the downstream distance along the centerline with high intensity are marked by the dashed lines. It can be seen that beyond a certain axial distance, no droplets are seen in both cases. This can be attributed to the existence of the flame that leads to the vaporization of all droplets within this region. Overall, the simulation spray distribution closely resembles the experimental distribution and captures the regions of low and high intensity well.

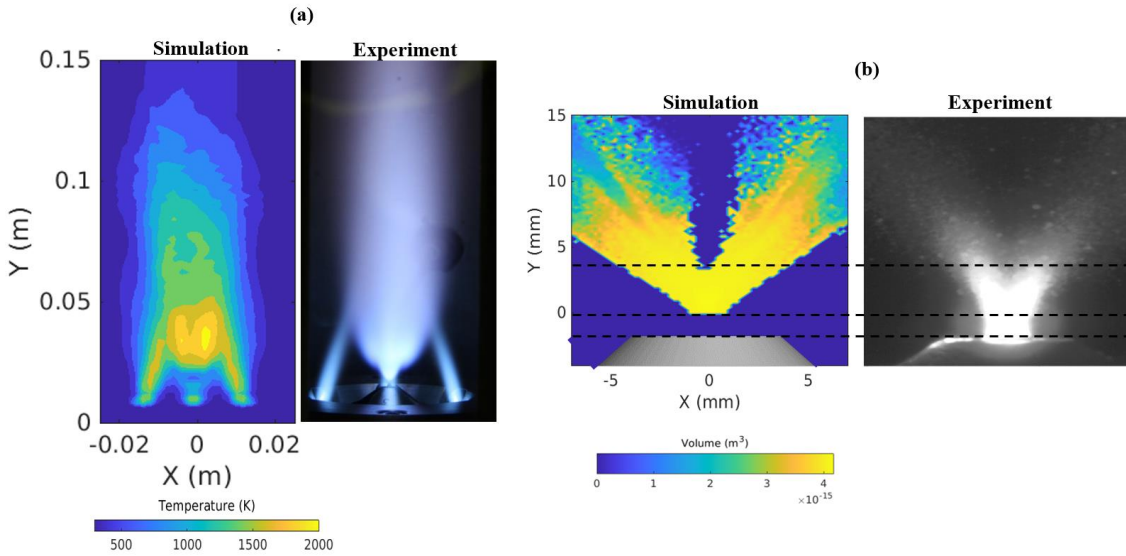


Figure 8. Comparison between simulations and experiments for (a) flame shape (simulations shown by averaged line-of-sight integrated temperature contours, experiment shown by flame luminescence image) (b) reacting spray distribution (experiment shown by averaged laser scattered image of the central plane, simulations shown by averaged droplet volume at the central plane). The three dashed lines represent the nozzle exit, the simulation spray initialization location, and the downstream distance along the centerline with high intensity.

### 3.4 Flame shape comparison

The flame dynamics play a crucial role in determining the spatial distribution of the high and low temperature regions that, in turn, influence the particle nucleation, growth, and agglomeration. Figure 9 shows the temperature contours for the four different cases considered in this study. It can be observed that changing the flow rate for the different inputs parameters can significantly change the local flow-field leading to different flame shapes even if one or two of the parameters are similar. For example, between Case 2 and Case 3, the pilot flow rate (6.0 L/min vs. 6.3 L/min) and sheath oxygen flow rate (17 L/min vs. 18 L/min) are similar. However, the difference in the dispersion oxygen flow rates and liquid flow rates lead to varied shapes. For Case 2, the high temperature regions ( $T > 2000$  K) appear as spray flame branches. For Case 3, on the other hand, it can be seen that the branches merge leading to central high temperature region. Increasing the dispersion and liquid flow rates enhances the local mixing of the vaporized precursor/solvent mixture and the oxygen leading to higher temperatures along the centerline. Another observable difference in the flame shape is the width of the flames. As can be seen, Case 2 has the least flame width. In comparison, Case 3 has the widest flame shape. This change is due to the increased dispersion and liquid flow rate. The subsequent sections discuss these flame dynamics in more details for the different input parameters and how they can potentially impact the particle sizes and their distribution.

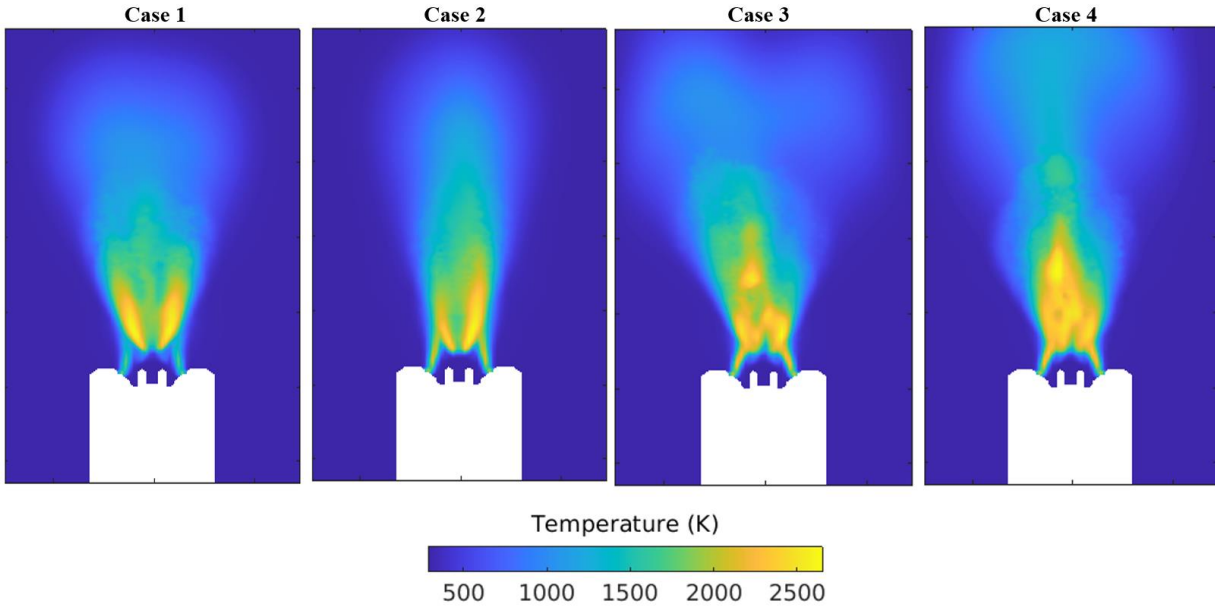


Figure 9.  $Z=0$  mm plane averaged temperature contours for the four cases. Each contour is titled with the case number.

### 3.5 Effect of precursor concentration

The flame shape determines the spatial regions conducive for particle formation and growth. The high temperature favors the fast pyrolysis of the precursor into the gaseous phase oxides that lead to the formation of the nanoparticles through nucleation. This can be seen in Figure 10 where the regions of non-zero particle mass fraction due to nucleation conform to the flame shape outlined by the 1800-K isotherm. Another point to note here is that decreasing the precursor concentration decreases the particle mass fraction. To further quantify the change in particle sizes, statistics for the sizes and their distribution are extracted from the simulations and compared with experiments.

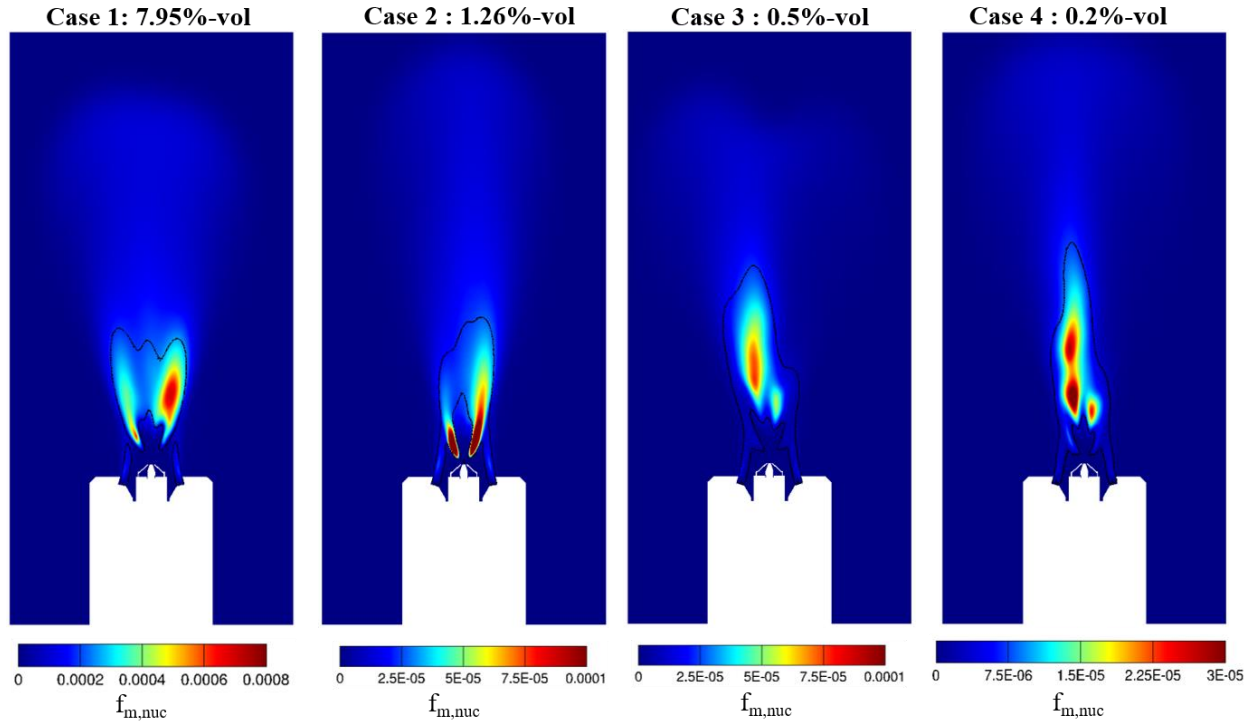


Figure 10. Particle mass fraction due to nucleation ( $f_{m,nuc}$ ) contours on  $Z = 0$  mm plane for different cases titled with the case number and the corresponding precursor concentration at  $t=0.10$ s. The black contour line corresponds to the 1800-K isotherm.

The particles are sampled close to the outflow boundary of the reactor (height above the nozzle exit = 222.0 mm). The particle volume fraction (ratio between total volume of particles and reference gas volume) and the total particle surface area (ratio between total surface area of particles and reference gas volume) were used to calculate the particle diameter. Table 3 shows the mean and median particle sizes from the experiments and simulations. For the simulations, the nanoparticle median and mean sizes, along with the maximum variation of these quantities, are reported over a duration of 10 ms. Within the 10 ms time-frame, approximately 500 instants are sampled. Based on the average velocity at the sampling point, the 10 ms sampling time corresponds to approximately 5-6 flow-through times. Good qualitative and quantitative agreement can be seen between the predicted and measured nanoparticle size. The maximum variation seen is within 10% of the reported mean and median from the simulations.

Table 3. Comparison of median and mean particle diameter between experiments and simulations.

	Median (nm)		Mean (nm)	
	Experiment	Simulation	Experiment	Simulation
Case 1	<b>239.63</b>	<b>261.44 ± 15.74</b>	<b>289.03</b>	<b>328.72 ± 26.25</b>
Case 2	<b>117.59</b>	<b>109.02 ± 18.49</b>	<b>129.22</b>	<b>148.52 ± 17.27</b>
Case 3	<b>81.97</b>	<b>70.12 ± 5.93</b>	<b>88.47</b>	<b>111.89 ± 4.10</b>
Case 4	<b>48.35</b>	<b>59.92 ± 7.18</b>	<b>52.38</b>	<b>66.51 ± 5.61</b>

Paulson et al. [37] further processed the SMPS data as outlined in section 2.1 and calculated the mean and standard deviation from the log-normal fit. The data from the simulations, for each case, was also fit to a log-normal distribution as shown in Figure 11. The calculated mean and standard deviation from the fitted distribution and the equivalent experimental values are reported in Table 4.

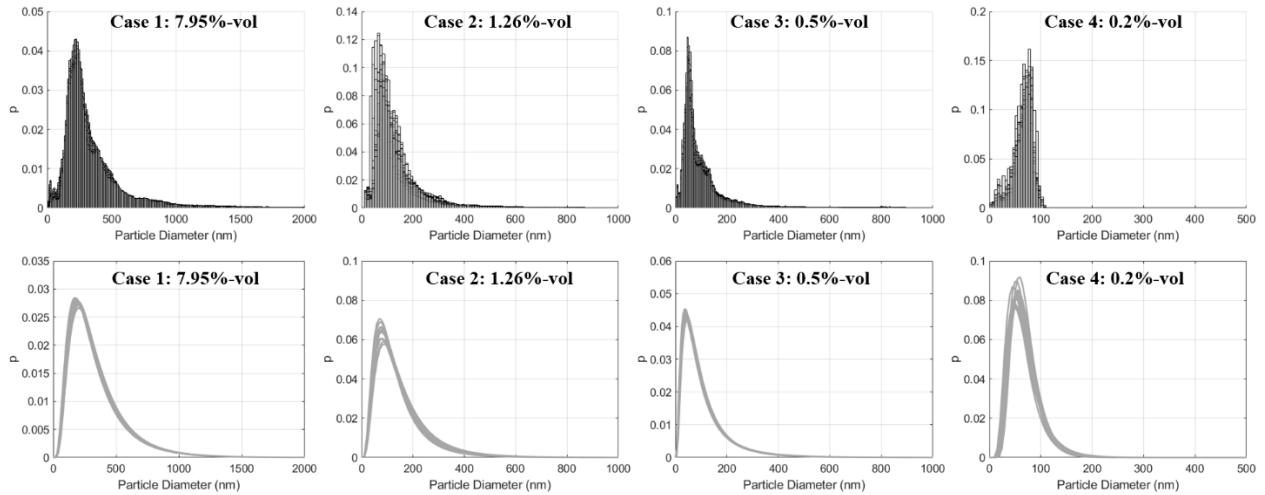


Figure 11. Histograms (top) and log-normal fit (bottom) for the particle size distribution overlaid for a time span of 10 ms sampled at 0.02 ms for all four cases.

Table 4. Comparison of log-normal fit mean and standard deviation between experiments and simulations.

	Mean, $\mu$ (nm)		Standard Deviation, $\sigma$ (nm)		$\sigma/\mu$	
	Experiment	Simulation	Experiment	Simulation	Experiment	Simulation
Case 1	<b>627.95</b>	<b>342.38</b> $\pm$ 19.75	<b>530.93</b>	<b>298.65</b> $\pm$ 12.69	0.85	0.87
Case 2	<b>163.77</b>	<b>155.66</b> $\pm$ 21.56	<b>80.79</b>	<b>77.36</b> $\pm$ 12.72	0.49	0.50
Case 3	<b>114.07</b>	<b>109.59</b> $\pm$ 3.97	<b>55.56</b>	<b>51.84</b> $\pm$ 10.25	0.48	0.47
Case 4	<b>70.52</b>	<b>68.53</b> $\pm$ 6.12	<b>37.12</b>	<b>30.91</b> $\pm$ 9.05	0.52	0.45

A strong dependence of the nanoparticle size on the precursor concentration can be seen from the data in Table 4. For Cases 2 to 4, there is reasonable quantitative agreement for all three quantities – namely, the mean, the standard deviation, and their ratio. For Case 1, the mean and standard deviation predicted by the simulations are approximately 1.7–1.8 times smaller than the corresponding experimental values. It should be noted that for this case, in both simulations and experiments, the standard deviations are large and very close to the mean itself. This, in turn, results in the ratio of standard deviation to mean close to 1 (cf. last two columns of Table 4). Moreover, for the lower precursor concentrations (Cases 2 to 4), this ratio remains constant around 0.5. Thus, at the lower concentrations (Cases 2-4,) the relative spread, given by the ratio of the standard deviation and mean, shows limited sensitivity to the concentration whereas for Case 1, that has a higher TEOS concentration, this spread is higher. At lower concentrations, the probability of particle collision is lower. Thus, the particles remain as primary particles or are isolated leading to smaller sizes. Increasing the concentration, increases the probability of collision among the particles leading to agglomeration and subsequently large sized particles.

### 3.6 Effect of pilot flow rate

The pilot flames are a critical component of the FSP system. They provide the initial hot environment that promotes vaporization of the liquid spray and subsequent ignition in the fuel vapor phase. From Figure 9, it can be observed that the pilot flames become longer as the pilot flow rate increases. This observation is further confirmed by plotting the temperature as a function of the distance from the pilot port exits as shown in Figure 12. The plots are shown for the two pilots whose centroids lie on the  $Z = 0$  mm plane. For each case, the temperature first increases

indicating the pilot flame and its stabilization. The profile then shows a decline as the temperature decreases through the pilot flame due to the dilution of the hot products by the surrounding sheath-oxygen flow. Thereafter, the temperature again rises and decreases as the sample line crosses the spray flame branches. With increasing pilot flow rates, the pilot flame tends to stabilize further downstream. This behavior can be observed by estimating the distance over which the temperature increases from 300K to  $\sim 3000$ K near the pilot exit. For example, for Case 1, with the lowest pilot flow rates, the first temperature rise occurs 0.6 mm downstream of the pilot exit followed by Case 2 at 1.7 mm, Case 3 at 2.3 mm, and Case 4 at 2.8 mm. Increasing the flow rates also leads to longer flames and an increased penetration of the pilot flames towards the central spray region. For shorter flames (i.e., Case 1), the temperature drops to  $\sim 1000$ K after the first peak. This drop is much larger compared to longer flames. For example, for Case 4 the temperature drops to only  $\sim 2400$ K. This behavior directly impacts the ignition point of the spray flame during its transient development stage. While the pilot flames do not directly influence the particle sizes and their distribution, they impact the spray flame shape. Increasing the pilot flow rates can have a secondary influence on the spray flame anchoring and spray flame height. Changes in the spray flame shape leads to varied spatial distributions of temperature within the reactor. These changes can, subsequently, impact the distribution of the nanoparticles formed within the reactor since it is known that this process is temperature sensitive.

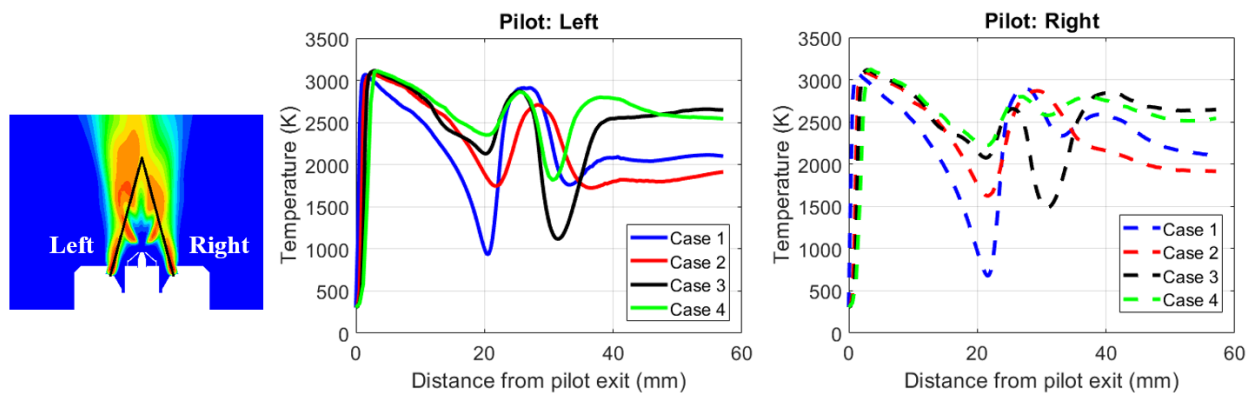


Figure 12. Variation of temperature with distance from the pilot exit at  $t=0.15$ s for all cases. The contour image for Case 4 at  $t=0.015$ s is provided to show the normal along which temperature profiles are extracted.

### 3.7 Effect of dispersion oxygen flow rate

To understand the impact of the dispersion oxygen flow rate, cases 2 to 4 are considered. Since the sheath oxygen flow rate is relatively similar for these cases, the impact of the dispersion oxygen on the spray flame and its stabilization can be isolated. To estimate the flame anchoring location, the surface defined by the 2400-K isotherm is utilized. This is shown in Figure 13(a). The lowest point on the central iso-surface (with respect to the  $y$ -coordinate, shown in Figure 13(b)) is termed as the flame anchoring location. This location is identified for all the three cases and is shown in Figure 13(c). It can be observed that increasing the dispersion oxygen flow rate results in the displacement of the flame anchoring locations further downstream of the nozzle exit. In addition, a larger difference in flow rate leads to a larger change in the anchoring location. For example, the flow rate of Case 4 (i.e., 10.5 L/min) is 4.2 L/min higher than that of Case 2 (i.e., 6.3 L/min), leading to a height difference of  $\sim 2$  mm, whereas the flow rate of Case 3 (i.e., 11.7 L/min) is only 1.2 L/min higher than that of Case 4 leading to a height difference of  $\sim 1$  mm. This monotonic change can likely be attributed to the increased momentum from the dispersion flow rate. Increasing the dispersion oxygen flow rate results in higher momentum exchange between the gas phase and the spray droplets as they atomize and vaporize in the central region of the domain. As a result, the spray flame anchoring location moves downstream with increasing flow rate.

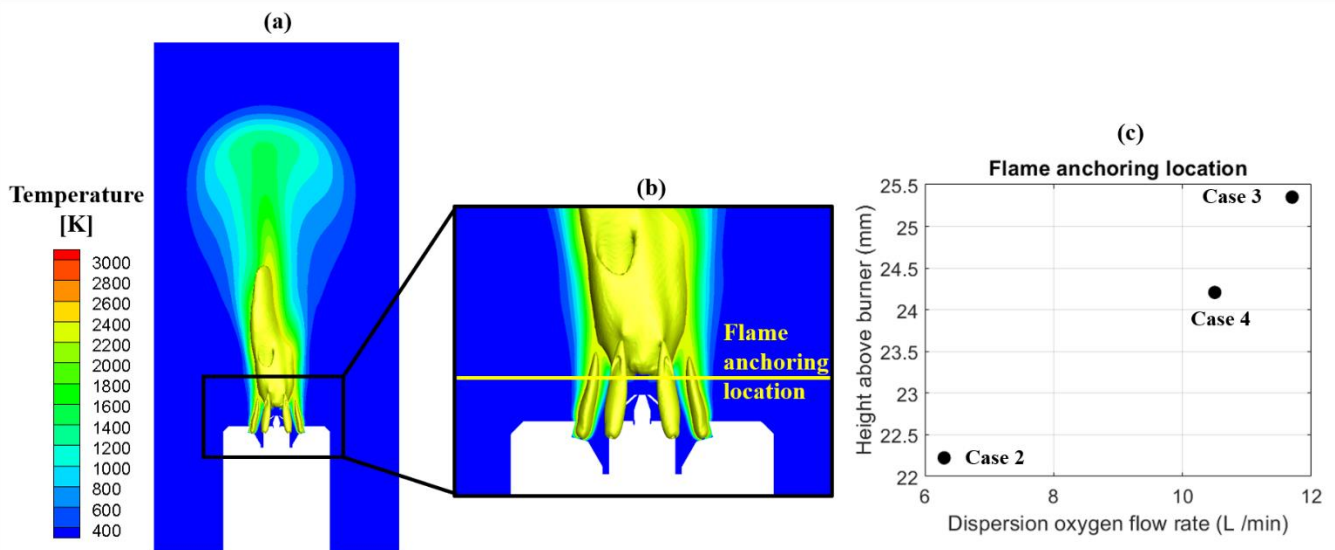
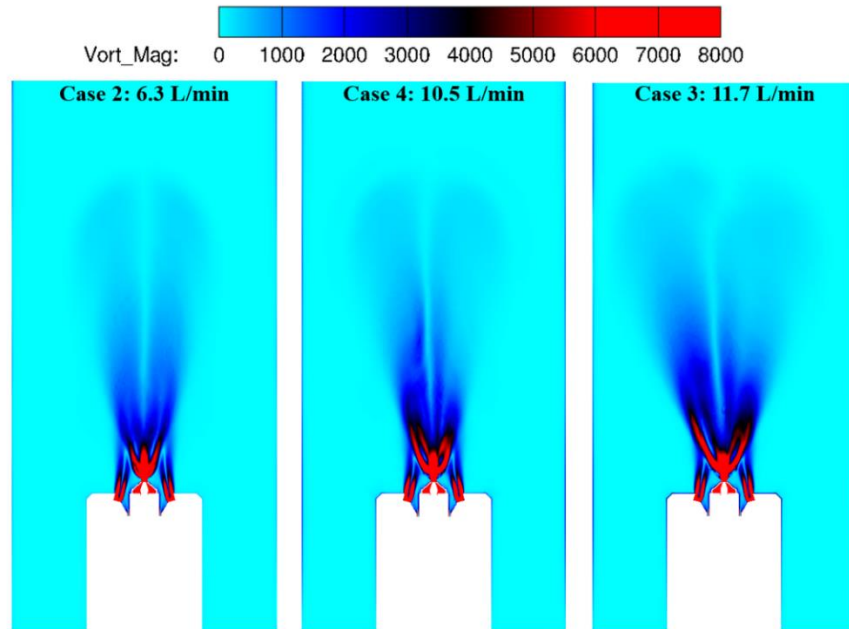


Figure 13. (a) Instantaneous Temperature contour at  $Z = 0$  mm plane with 2400-K iso-surface for Case 4 at  $t=0.1s$ . (b) Identification of the lowest point on the iso-surface with respect to the  $y$  coordinate (c) Plot of flame anchoring location vs. dispersion oxygen flow rate at  $t=0.1s$

Figure 14 shows the vorticity contours on the  $Z = 0$  mm plane. Increasing the dispersion flow rate leads to velocity gradients extended over a larger volume of the domain suggesting enhanced mixing downstream of the burner. This has a direct impact on the spray flame shape and its spread as discussed next.



*Figure 14. Instantaneous vorticity contours on  $Z = 0$  mm plane for Cases 2-4 at  $t=0.1$ s. Each contour is titled with the case number and the corresponding dispersion oxygen flow rate.*

The flame shape and spread are estimated by calculating the flame width at three distances (2 mm, 4 mm, and 8 mm) downstream of the flame anchoring location as shown in Figure 15(a). Firstly, the temperature profiles are extracted along the radial direction at these distances (shown in Figure 15(b)). Next, the profile width is calculated for two isotherms: 1000 K and 1600 K. This width is estimated by calculating the distance between the two points where the isotherms and the profiles intersect. For both isotherms, the flame width shows an increase with increasing flow rates at all distances. The enhanced mixing over a larger volume leads to wider flames at all distances downstream of the anchoring location. For the 1000-K isotherm, it can be noted that flame width varies monotonically with increasing downstream distance for any given case, suggesting a V-type shape for this isotherm. On the other hand, at 1600 K, the flame width at 8 mm shows values that are lower than those at 4 mm suggesting a slightly different shape of the higher-temperature inner

region for the spray flames. Nevertheless, the trend of increasing flame width with increasing dispersion oxygen flow rate remains consistent across all distances and isotherms.

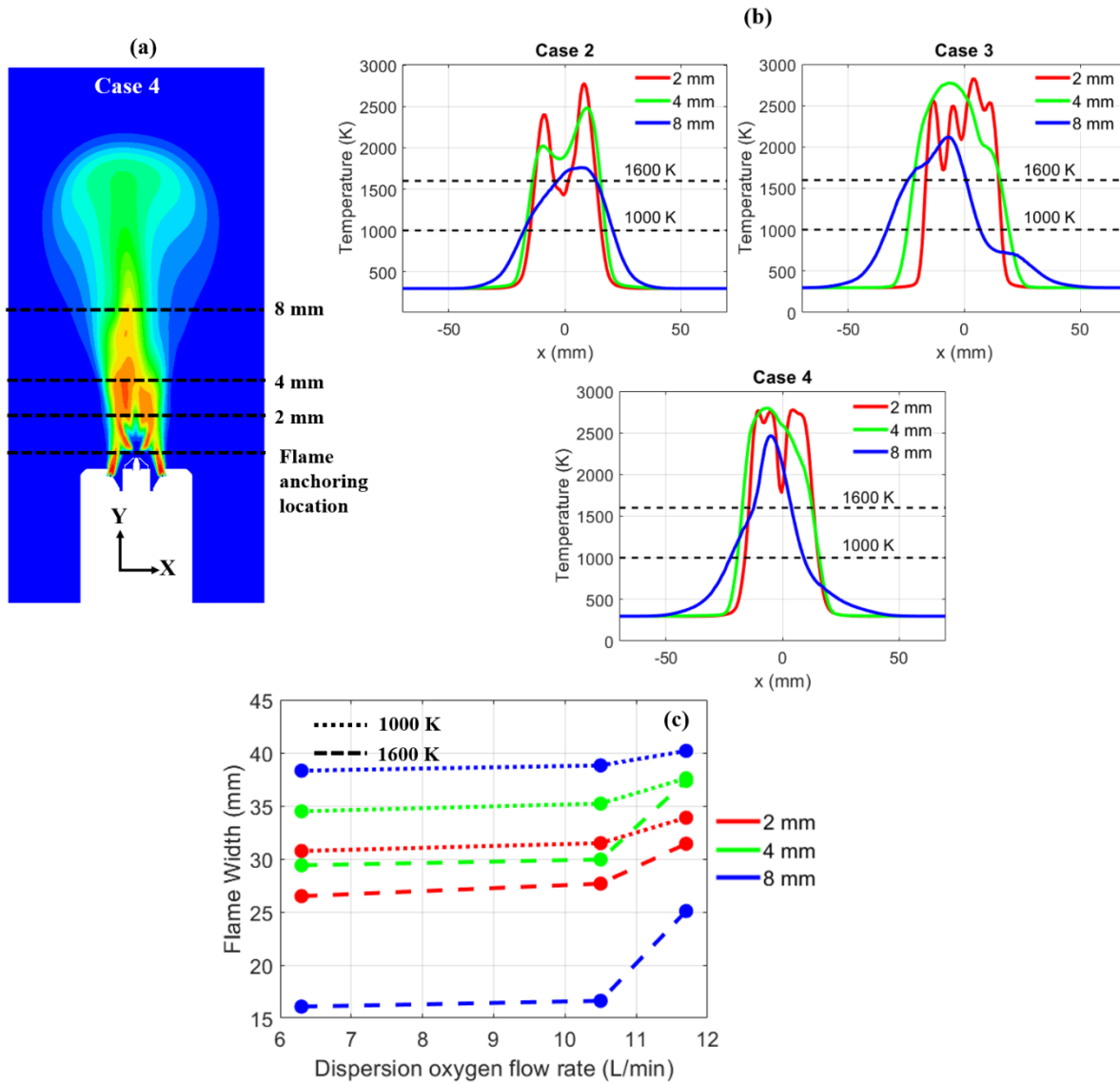


Figure 15. (a)  $Z = 0$  mm temperature contour at  $t = 0.1$  s for Case 4 with locations for temperature profile extraction; (b) radial temperature distribution for Cases 2 to 4 at 2 mm, 4 mm, and 8 mm downstream of the flame anchoring location with 1000-K and 1600-K isotherms at  $t = 0.1$  s; (c) variation of flame width with dispersion oxygen flow rate at  $t = 0.1$  s.

Increasing dispersion flow rate leads to higher velocities near the nozzle exit resulting in enhanced mixing leading to wider and shorter flames. Additionally, the higher velocities also lead to reduced residence time of the particles formed due to nucleation in the high temperature zone. The reduced residence time can lead to reduced rate of growth of the particles. From Figure 9, it can be seen

that the flame shape changes with the increase in dispersion oxygen rate and leads to larger regions of high temperature close to the nozzle. These high temperature regions can increase the rate of particle growth. Thus, there are two competing physics, residence time and high temperature, that control the particle growth. By controlling the flame shape, one can control the particle growth allowing for an effective control of particle sizes produced within the FSP reactor.

#### **4 Conclusions**

An unsteady RANS CFD analysis of silica nanoparticle synthesis from FSP was presented in this work. A CFD model was developed to simulate the complex burner geometry with different operating conditions to capture the relevant physics with the goal of understanding the multi-physics interactions within the burner. Four cases were presented with varying inflow rates for the pilot flow, dispersion oxygen flow, sheath oxygen flow, liquid flow rate, and concentration of precursor in the solvent. The particle sizes and distributions predicted by the CFD model were shown to be in good agreement with experimental measurements. The analysis of simulation results primarily focused on the effects of pilot flow rate, dispersion oxygen flow rate, and precursor concentration on the internal reactor dynamics. It was observed that increasing the pilot flow rate increased the length of the pilot flame and its penetration into the central region facilitating an improved ignition of the spray flame resulting in a secondary influence on the flame shape. The impact of dispersion oxygen was two-fold. Firstly, it played a critical role in determining the spray flame stabilization location with higher flow rates pushing the flame further downstream. It can be speculated that if this flow rate were to increase beyond a certain point, the flame stability may be compromised. Secondly, increasing the dispersion-oxygen flow rate expanded the local mixing zone downstream of the spray nozzle leading to wider flames and larger regions of particle formation. Using the dispersion flow rate, the flame shape can be controlled. This shape helps determine the regions of high temperature and the residence time of the particles in the high temperature region. Controlling the flame shape can allow for a control of the particle growth and hence its size and distribution. While these flow rates determined the major flow and flame dynamics, the precursor concentration determined the eventual size of the nanoparticles generated. There was a direct correlation between these two quantities i.e., increasing the precursor's concentration led to larger particles. This is attributed to the increased probability of collision and subsequent agglomerate particle formation. At lower concentrations, the collision

probability is low, leading to smaller particle sizes. Additionally, because of this, the spread of the particle size distribution shows limited sensitivity to concentration at lower levels.

The FSP process can access a large range of flow rates for all the input parameters. As part of our future work, the analysis will be extended to explore a larger parameter space. Additionally, the large-scale data generated will be used for creating a reduced-order model of the MERF's FSP reactor with the goal of incorporating the relevant physics that can enable a near real-time optimization of the FSP system for use in large-scale nanoparticle synthesis.

## **5 Acknowledgements**

The submitted manuscript has been created by UChicago Argonne, LLC, Operator of Argonne National Laboratory (Argonne). Argonne, a U.S. Department of Energy (DOE) Office of Science laboratory, is operated under Contract No. DEAC02-06CH11357. The U.S. Government retains for itself, and others acting on its behalf, a paid-up nonexclusive, irrevocable world-wide license in said article to reproduce, prepare derivative works, distribute copies to the public, and perform publicly and display publicly, by or on behalf of the Government. This research was supported by Laboratory Directed Research and Development (LDRD) funding from Argonne National Laboratory, provided by the Director, Office of Science, of the U.S. Department of Energy under contract LDRD Prime 2019-0254. The CFD simulations were performed using computing resources provided on Bebop, a high-performance computing cluster operated by the Laboratory Computing Resource Center (LCRC) at Argonne. Lastly, the authors wish to thank Convergent Science, Inc. for providing the CONVERGE software licenses.

## **6 References**

- [1] W.Y. Teoh, R. Amal, L. Mädler, Flame Spray Pyrolysis: An enabling technology for nanoparticle design and fabrication, *Nanoscale* 2 (2010) 1324-1347.
- [2] H.K. Kammler, L. Mädler, S.E. Pratsinis, Flame synthesis of nanoparticles, *Chem. Eng. Technol.* 24 (2001) 583-596.
- [3] G. Solero, Synthesis of Nanoparticles through Flame Spray Pyrolysis: Experimental Apparatus and Preliminary Results, *J. Nanosci. Nanotechnol.* 7 (2017) 21-25.

- [4] J. W. Carroz, F. K. Odencrantz, W.G. Finnegan, D.C. Drehmel, Aerosol generation to simulate specific industrial fine particle effluents, *Am. Ind. Hyg.* 41 (1980) 77-84.
- [5] C. Weise, J. Menser, S. A. Kaiser, A. Kempf, I. Wlokas, Numerical investigation of the process steps in a spray flame reactor for nanoparticle synthesis, *Proc. Combust. Inst.* 35 (2015) 2259-2266.
- [6] A. Kilian, T.F. Morse, A novel aerosol combustion process for the high rate formation of nanoscale oxide particles, *Aerosol Sci. Technol.* 34 (2001) 227-235.
- [7] L. Mädler, W.J. Stark, S. E. Pratsinis, Flame-made ceria nanoparticles, *J. Mater. Res.* 17 (2002) 1356-1362.
- [8] C. Schulz, T. Dreier, M. Fikri, H. Wiggers, Gas-phase synthesis of functional nanomaterials: Challenges to kinetics, diagnostics, and process development, *Proc. Combust. Inst.* 37 (2019) 83-108.
- [9] B. Buesser, S.E. Pratsinis, Design of Nanoparticle Synthesis by Aerosol Processes, *Annu. Rev. Chem. Biomol. Eng.* 3 (2012) 103-127.
- [10] F. Meierhofer, L. Mädler, U. Fritsching, Nanoparticle evolution in flame spray pyrolysis-Process design via experimental and computational analysis, *AIChE J* 66 (2020) 1-14.
- [11] D. Kilian, S. Engel, B. Borsdorf, Y. Gao, A.F. Kogler, S. Kobler, T. Seeger, S. Will, A. Leipertz, W. Peukert, Spatially resolved flame zone classification of a flame spray nanoparticle synthesis process by combining different optical techniques, *J. Aerosol Sci.* 69 (2014) 82-97.
- [12] S. R. Engel, A.F. Kogler, Y. Gao, D. Kilian, M. Voigt, T. Seeger, W. Peukert, A. Leipertz, Gas phase temperature measurements in the liquid and particle regime of a flame spray pyrolysis process using O<sub>2</sub>-based pure rotational coherent anti-stokes Raman scattering, *J. Opt. Soc. Am.* 51 (2012) 6063-6075.
- [13] S.K. Friedlander, *Smoke, Dust, And Haze, Fundamental of Aerosol Dynamics*, Oxford University Press (2000).
- [14] M. Frenklach, Dynamics of discrete distribution for Smoluchowski coagulation model, *J. Colloid Interface Sci.* 108 (1985) 237-242.
- [15] S. Tsantilis, H.K. Kammler, S.E. Pratsinis, Population balance modeling of flame synthesis of titania nanoparticle, *Chem. Eng. Sci.* 57 (2002) 2139-2156.

- [16] M. Frenklach, S.J. Harris, Aerosol dynamics modeling using the method of moments, *J. Colloid Interface Sci.* 118 (1987) 252-261.
- [17] R. Fan, D. L. Marchisio, R. O. Fox, Application of the direct quadrature method of moments to polydisperse gas-solid fluidized beds, *Powder Technol.* 139 (2004) 7-20.
- [18] J. Akroyd, A.J. Smith, L.R. McGlashan, M. Kraft, Numerical investigation of DQMoM-IEM as a turbulent reaction closure, *Chem. Eng. Sci.* 65 (2010) 1915-1924.
- [19] Y. Sung, V. Raman, H. Koo, M. Mehta, R.O. Fox, Large-Eddy Simulation Modeling of Turbulent Flame Synthesis of Titania Nanoparticle Using a Bivariate Particle Description, *AIChE J* 60 (2014) 459-472.
- [20] F.E. Kruis, K.A. Kusters, S.E. Pratsinis, B. Scarlett, A Simple Model for the Evolution of the Characteristics of Aggregate Particles Undergoing Coagulations and Sintering, *Aerosol Sci. Technol.* 19 (1993) 514-526.
- [21] A.J. Gröhn, S. E. Pratsinis, K. Wegner, Fluid-particle dynamics during combustion spray aerosol synthesis of  $ZrO_2$ , *Chem. Eng. J.* 191 (2012) 491-502.
- [22] A. Rittler, L. Deng, I. Wlokas, A.M. Kempf, Large eddy simulations of nanoparticle synthesis from flame spray pyrolysis, *Proc. Combust. Inst.* 36 (2017) 1077-1087.
- [23] D. Noriler, M. J. Hodapp, R. K. Decker, H. F. Meier, F. Meierhofer, U. Fritsching, Numerical Simulation of Flame Spray Pyrolysis Process for Nanoparticle Productions: Effects of 2D and 3D Approaches, *Proceedings of the ASME 2014 4th Joint US-European Fluids Engineering Division Summer Meeting (2014)*, Chicago, Illinois, USA.
- [24] P. B. Neto, L. Buss, F. Meierhofer, H. F. Meier, U. Fritsching, D. Noriler, Combustion kinetic analysis of flame spray pyrolysis process, *Chem. Eng. Process* 129 (2018) 17-27.
- [25] F. Schneider, S. Suleiman, J. Menser, E. Borukhovich, I. Wlokas, A. Kempf, H. Wiggers, C. Schulz, SpraySyn—A standardized burner configuration for nanoparticle synthesis in spray flames, *Rev. Sci. Instrum.* 90 (2019) 085108.
- [26] P. Wollny, S. Angel, H. Wiggers, A. M. Kempf, I. Wlokas, Multiscale Simulation of the Formation of Platinum-Particles on Alumina Nanoparticles in a Spray Flame Experiment, *Fluids* 5 (2020) 201.
- [27] A. Abdelsamie, F. E. Kruis, H. Wiggers, D. Thévenin, Nanoparticle Formation and Behavior in Turbulent Spray Flames Investigated by DNS, *Flow Turbul. Combust.* 105 (2020) 497-516.

- [28] L. Cifuentes, J. Sellmann, I. Wlokas, A. Kempf, Direct numerical simulations of nanoparticle formation in premixed and non-premixed flame–vortex interactions, *Phys. Fluids*, 32 (2020), 093605
- [29] A. Abdelsamie, C. Chi, M. Nanjaiah, I. Skenderović, S. Suleiman, D. Thévenin, Direct Numerical Simulation of Turbulent Spray Combustion in the SpraySyn Burner: Impact of Injector Geometry, *Flow Turbul. Combust.* 106 (2021) 453-469.
- [30] R. Mueller, L. Mädler, S.E. Pratsinis, Nanoparticle synthesis at high production rates by flame spray pyrolysis, *Chem. Eng. Sci.* 58 (2003) 1969-1976.
- [31] H. Torabmostaedi, T. Zhang, Numerical simulation of TiO<sub>2</sub> nanoparticle synthesis by flame spray pyrolysis, *Powder Technol.* 329 (2018) 426-433.
- [32] H. Torabmostaedi, T. Zhang, P. Foot, S. Dembele, C. Fernandez, Process control for the synthesis of ZrO<sub>2</sub> nanoparticles using FSP at high production rate, *Powder Technol.* 246 (2013) 419-433.
- [33] H. Torabmostaedi, T. Zhang, Effect of nozzle geometry and processing parameters on the formation of nanoparticles using FSP, *Chem. Eng. Res. Des.* 92 (2014) 2470-2478.
- [34] M. Bieber, M. Al-Khatib, F. Fröde, H. Pitsch, M. A. Reddemann, H-J. Schmid, R. Tischendorf, R. Kneer, Influence of angled dispersion gas on coaxial atomization, spray and flame formation in the context of spray-flame synthesis of nanoparticles, *Exp. Fluids* 62 (2021) 98.
- [35] L. Mädler, H.K. Kammler, R. Mueller, S.E. Pratsinis, Controlled synthesis of nanostructured particles by flame spray pyrolysis, *J. Aerosol Sci.* 33 (2002) 369-389.
- [36] P. Virtanen, R. Gommers, T.E. Oliphant, M. Haberland, T. Reddy, D. Cournapeau, E. Burovski, P. Peterson, W. Weckesser, J. Bright, S.J. van der Walt, M. Brett, J. Wilson, K.J. Millman, N. Mayorov, A.R.J. Nelson, E. Jones, R. Kern, E. Larson, C.J. Carey, Í. Polat, Y. Feng, E.W. Moore, J. VanderPlas, D. Laxalde, J. Perktold, R. Cimrman, I. Henriksen, E.A. Quintero, C.R. Harris, A.M. Archibald, A.H. Ribeiro, F. Pedregosa, P. van Mulbregt, and SciPy 1.0 Contributors, *SciPy 1.0: Fundamental Algorithms for Scientific Computing in Python*, *Nat. Methods* 17 (2020) 261-272.
- [37] N. H. Paulson, J. A. Libera, M. Stan, Flame spray pyrolysis optimization via statistics and machine learning, *Mater. Des.* 96 (2020) 108972.
- [38] K. J. Richards, P. K. Senecal, E. Pomraning, CONVERGE 2.4.26, Convergent Science, Madison, WI (2000).

- [39] N.M. Marinov, A Detailed Chemical Kinetic Model for High Temperature Ethanol Oxidation, *Int. J. Chem. Kinet.* 31 (1999) 183-220.
- [40] D. Nurkowski, P. Buerger, J. Akroyd, M. Kraft, A detailed kinetic study of the thermal decomposition of the Tetraethoxysilane, *Proc. Combust. Inst.* 35 (2015) 2291-2298.
- [41] V. Yakhot, S.A. Orszag, S. Thangam, T. B. Gatski, C. G. Speziale, Development of turbulence models for shear flows by a double expansion technique, *Phys. Fluid A: Fluid Dyn.* 4 (1992) 1510-1520.
- [42] C.W. Hirt, B.D. Nichols, Volume of fluid (VOF) method for the dynamics of free boundaries, *J. Comput. Phys.* 39 (1981) 201-255.
- [43] T. Waclawczyk, T. Koronowicz, Modeling of the Wave Breaking CICSAM and HRIC High-Resolution Scheme, *ECCOMAS CFD (2006)*, TU Delft, The Netherlands.
- [44] P.J. O'Rourke, A.A. Amsden, The TAB Method for Numerical Calculation of Spray Droplet Breakup, *SAE (1987) Paper 872089*.
- [45] A. A. Amsden, P. J. O'Rourke, T. D. Butler, *KIVA-II: A Computer Program for Chemically Reactive Flows with Sprays*, Los Alamos National Laboratory Technical Report LA-11560-MS (1989).
- [46] K. J. Richards, P. K. Senecal, E. Pomraning, *CONVERGE 3.0 Manual*, Convergent Science, Madison, WI (2021).
- [47] S. Tsantilis, H. Briesen, S.E. Pratsinis, Sintering Time for Silica Particle Growth, *Aerosol Sci. Technol.* 34 (2001) 237-246.
- [48] D. Dasgupta, P. Pal, R. Torelli, S. Som, Computational Fluid Dynamics Modeling of Flame Spray Pyrolysis for Nanoparticle Synthesis, *CSSCI Spring Technical Meeting (2020)*, Huntsville, Alabama.
- [49] E. Pomraning, Development of Large Eddy Simulation Turbulence Models, Ph.D. Thesis, University of Wisconsin-Madison, Madison, WI (2000).
- [50] J.C. Lasheras, E.J. Hopfinger, Liquid Jet Instability and Atomization in a coaxial gas stream, *Annu. Rev. Fluid Mech.* 32 (2000) 275-308.
- [51] M. F. B. Stodt, J. Kiefer, U. Fritsching, Drop Dynamics in heterogeneous spray flames for nanoparticle synthesis, *Atomization Spray* 30 (2020) 779-797.

